FR 8300848

6. International workshop on laser interaction and
related plasma phenomena
Monterey, CA, USA 25 - 29 Oct 1982
CEA-CONF--6562

HIGH DENSITY TRANSITION LASER DRIVEN IMPLOSIONS

C. Bayer, D. Billon, M. Decroisette, D. Juraszek,
D. Meynial
Centre d'Etudes de Limeil, B.P. n° 27, 94190 Villeneuve-Saint-Georges, France.

INTRODUCTION

In the scheme of inertial confinement fusion, the conditions for fuel ignition have to be economically achieved by applying an isentropic compression. For laser fusion, required final densities range between 10^3 to 10^4 times the liquid fuel density /1/.

First experiments in the field have been often performed with so-called exploding pusher targets /2-7/ interests of which being manyfold : easy manifacturing of the pellet, a bare DT filled glass microballoon ; simply described behaviour /8-11/ lying on a strong emission of suprathermal electrons leading to a rapid increase of temperature and the explosion of the shell ; relative insensitiveness to hydrodynamic instabilities and irradiation defects, authorizing simple focusing devices ; a low areal density at the end of compression, insuring an easy detection of any core emission (neutrons, α particles and X-rays), and thus a precise analysis of the implosion.

As final densities are low - a few 1/10 g.cm^{-3} - , efforts were oriented towards ablation ; the objective is to progressively compress the fuel by an unexpanded pusher, and to preserve it from preheating.

The two methods generally proposed for reducing preheat are : on one hand, a high Z screen in the pusher, or at least a thicker target wall , on the other hand, a reduction of fast electron generation, obtained by lowering the irradiance or employing shorter wavelength : this last solution appears very attractive, as providing in the same time high absorption rate and low preheat ratio /12-15/. In any case, a precise knowledge of electron transport is necessary. Recent experimental and theoretical works give some evidence that fast electrons are preferentially emitted towards the underdense plasma, and trapped in a rapidly expanding suprathermal corona ; as a consequence, temporal evolution of the preheat may differ from that of the laser pulse.

In an ablative implosion, leading to high density and low temperature of the core (fuel and compressed pusher), and thus to high $\int \rho dr$ values, conventional diagnostics such as X-rays imaging are no more suitable and other techniques like X-ray shadowgraphy [23] or neutron activation [24] have to be developped.

Several laboratories have been involved in so-called transition implosions, where both lengthening of the laser pulse and thickening of the pusher wall lead to a more ablative regime than the exploding pusher one [25,30]. Our first results in this field have been obtained with the Nd-glass facility C6, allowing a tetrahedral irradiation of DLi microspheres and neon-filled microballoons [31]. The experiments we present here, have been realized with the eight beams laser facility Octal [32,33] delivering 500 ps duration 1.06 µm pulses (Fig. 1), and plastic coated glass microballoons irradiated in cubic geometry ; high densities ($10 \times \rho_{liq\ DT}$) achieved with the thicker pellets have required an X-ray shadowgraphy probing system, which is described elsewere [23].

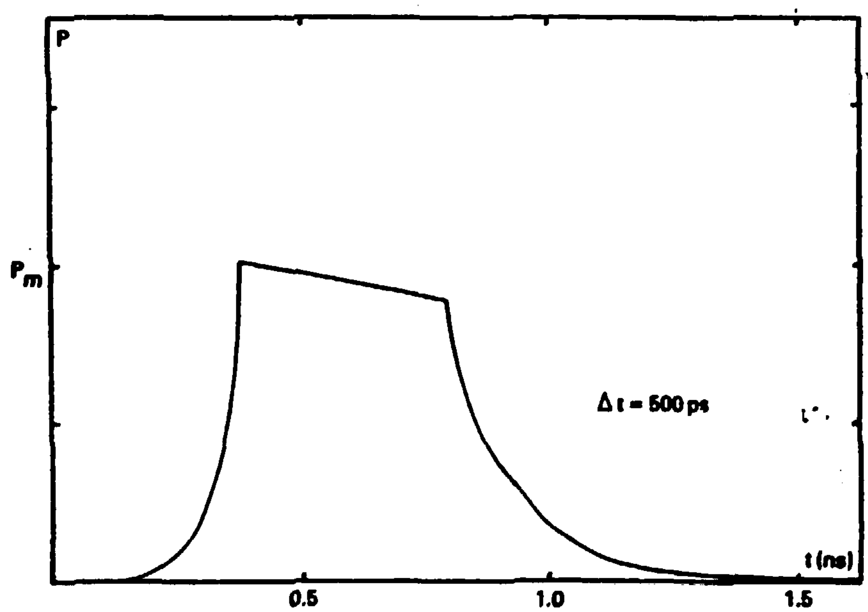

Fig. 1 Typical laser pulse-shape recorded with an Imacon infared camera (FWHM = 500 ps).

EXPERIMENTAL AND NUMERICAL MEANS

Experimental Set-Up

The eight f/1.5 lenses allow a nearly uniform energy deposition for d/R = 2, where d is the distance between best focus and target center, and R the target radius [7]. Essential diagnostics mounted on the interaction chamber concern I.R. calorimetry, charged particles collection, neutron detection, and X-rays emission in the 1-10 keV range ; as previously said, X-ray shadowgraphy was developped in order to study the hydrodynamical behaviour of nearly ablative implosions, for which self emissions from the core are slightly detectable as the temperature is low and $\int \rho dr$ high [23].

Targets

Experiments described here have been performed with glass microballoons 120 µm in diameter, 1 µm thick, filled with equimolar D.T. at pressure up to 25 bars ; the wall thickness was increased up to 8 µm by plastic coating [32-33].

Numerical Restitutions have been performed with our one dimensional lagrangian code FCI1 (one fluid, two temperatures) which is provided with several subroutines allowing to simulate experimental diagnostics such as X-ray pinhole photography and time-resolved X-ray shadowgraphy ; the thermal heat flux is given by the harmonic mean of the classical spitzer thermal flux [34] and of the inhibited thermal flux Q_L

$$Q_L = f \times 0.64 \times n_e \, k \, T_e \left(\frac{kT_e}{m_e}\right)^{1/2}$$

f is a free parameter in the code ; it has been kept equal to 5.10^{-2} for all the simulations presented here. The radiative transfer is treated by a multigroup method with a varying Eddington factor ; X-ray line emission is not taken in account.

Suprathermal electron transport is simulated by a multigroup diffusion method with a limited flux insuring electrical neutrality at any time. Slowing down occurs through Coulomb collisions with thermal electrons. Self consistent electric field is not modeled, so fast ions generation ($v > 2.10^8$ cm.s^{-1}) is not treated. Suprathermal distribution function is assumed maxwellian, with

$$T_H = 62 \, . \, (\phi_i(t) \, \lambda^2/10^{17})^{.42} \, T_{e\,CR}^{.3}(t) + T_{eCR}(t)$$

where T_{eCR} is the thermal componant temperature in the vicinity of critical. In our cases, T_H was close to 10 keV.

There is presently no theoretical model providing with the fraction of absorbed energy carried away by fast electrons, which appears thus as a second free parameter in the code ; this energy is wasted either in collision processes in the denser part of the target, or in ion acceleration in the corona.

For long laser pulses, the corona extension is large enough that the probability for a suprathermal electron to preheat the dense pellet is small ; this induces a core-corona decoupling [35].

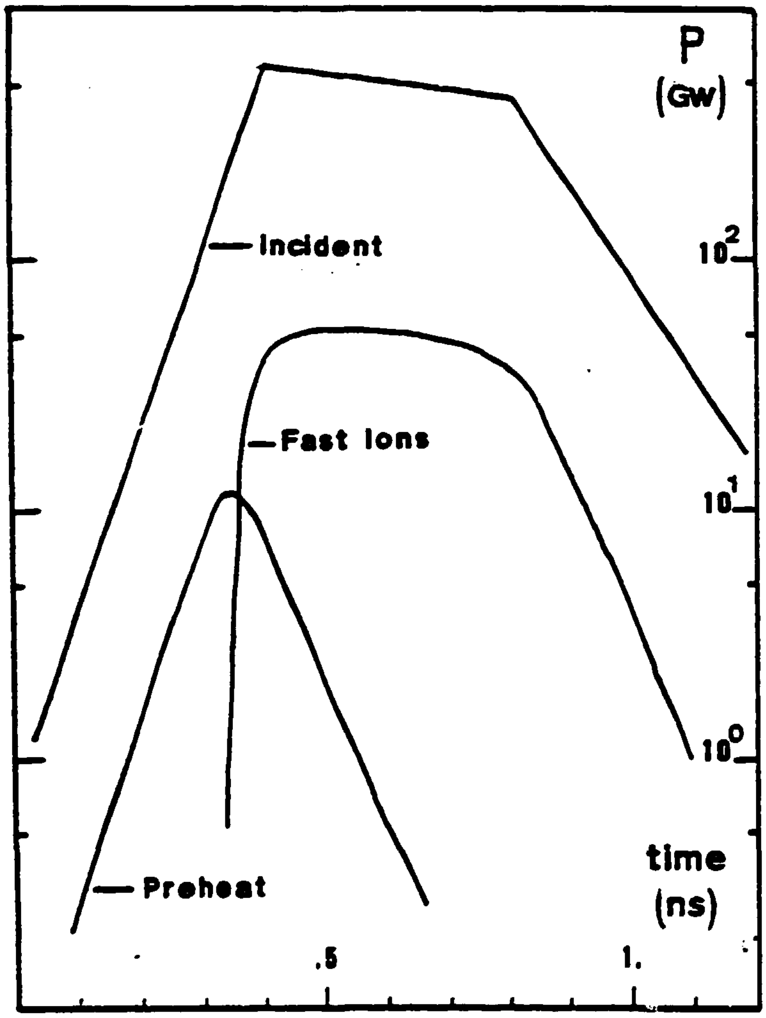

Fig. 2 Time dependance of the partition between preheat and fast ions acceleration introduced in the numerical simulations.

To simulate such an effect, we set in the code a preheat source decreasing in time, the rate being adjusted to provide a best fit of experimental results (Fig. 2). For 120 μm microballoons, 8.5 % of incident laser energy is attributed to fast electrons (i.e. 35 % of absorbed energy) ; around 8 % of this suprathermal energy is deposited into preheat, the remaining part is recovered into fast ions.

EXPERIMENTAL RESULTS AND NUMERICAL SIMULATIONS

We present here experimental results dealing with the influence of the shell thickness ΔR, for constant target diameter (2R), incident laser energy E_i) and DT pressure (ρ_{oDT}).

Table 1.

	D	E	F	G
2R μm	117	121	119	114
ΔR_{SiO2} μm	.95	.67	1	.81
ρo_{DT} $g.cm^{-3}$	5.10^{-3}	$5.4\ 10^{-3}$	$5.6\ 10^{-3}$	$5.3\ 10^{-3}$
ΔR_{CH} μm	0	3.8	5.5	8.2
E_a/E_i %	20 ± 5	22 ± 5	23 ± 5	24 ± 5
E fast ions/E_a %	30 ± 10	25 ± 10	25 ± 10	25 ± 10
Neutron Yields	2.10^5	$< 5.10^3$	$< 5.10^3$	$< 5.10^3$

Target characteristics as well as absorption efficiencies, fast ions energy ratios and neutron yields are reported in table 1.

Numerical simulations are initiated with target and laser pulse characteristics ; experimental energy balance deduced from ion and photon calorimetry define the deposited energy ; the final fittings are carried out by comparison with other experimental data, i.e. mainly the different X-ray emission and absorption recordings, and eventually the neutron yields.

Focusing conditions already mentionned insure a nearly uniform energy deposition, as evidenced by the X-ray pinhole picture (Fig. 3).

Fig. 4a presents the time resolved X-ray emission along a diameter of the bare microballoon (target D). Figs. 5a, 6a and 7a present the X-ray shadowgrams (time-resolved absorption picture along a diameter of the microballoon) for the plastic coated targets (E, F, G) ; in this cases, core and corona self emissions are very faint, so that the main data for comparison with numerical restitutions are the time resolved X-ray absorption profiles (timings of X-ray probing with respect to the laser pulse are shown in Figs. 5b, 6b and 7b).

Fig. 6a was obtained with three shots on identical targets but with different X-ray source timings (See Fig. 6b). The transmission limits in the shadowgrams, (outlines A in Figs. 5c, 6c and 7c) are defined within a ± 5 μm accuracy, due to the spatial resolution of the pinhole and to the noise in the recording, the dynamic of which (≃ 10) allowing not to discern strongly differing levels. Notice the double transmission profile which can be observed for the target G, whose transmission remains relatively high at the end of laser pulse (Fig. 7c).

These profiles have to be compared with the simulated iso-density contours (outlines A in Figs. 5d, 6d and 7d), defined as $I(r,t) = I_o(t) \times \tau(r,t) = \text{constant}$, where $I_o(t)$ stands for the source intensity at time t, and $\tau(r,t)$ for the target X-ray transmission. The X-ray source emission is assumed to be spatially uniform and to follow the same time evolution as the laser pulse :

$$I_o(t) = \frac{P(t - \Delta)}{P_M}$$

where P_M is the maximum laser power, and Δ the probing delay time.

Bare Microballoon (D)

Numerical simulations for glass-DT interface r-t diagram and iso-emission contours are presented Fig. 4d ; level ratio between the highest emission zone ($700 < t < 850$ ps) and the outer contour is ≃ 100. Comparison with Fig. 4c brings out that :

- the minimum of outer X-ray emission contour radius appears at t ≃ 850 ps, in agreement with experimental data ($t_{min} = 800 \pm 150$ ps) ;
- this time corresponds to the maximum DT compression ;
- within the experimental uncertainties, space-time evolution of X-ray emission is well restituted.

Coated targets (E, F, G)

Figs. 5d, 6d and 7d show the simulated r-t diagrams for glass-DT interface, induced shock in the fuel, and X-ray iso-transmission ($.1 < I/I_o < .2$).

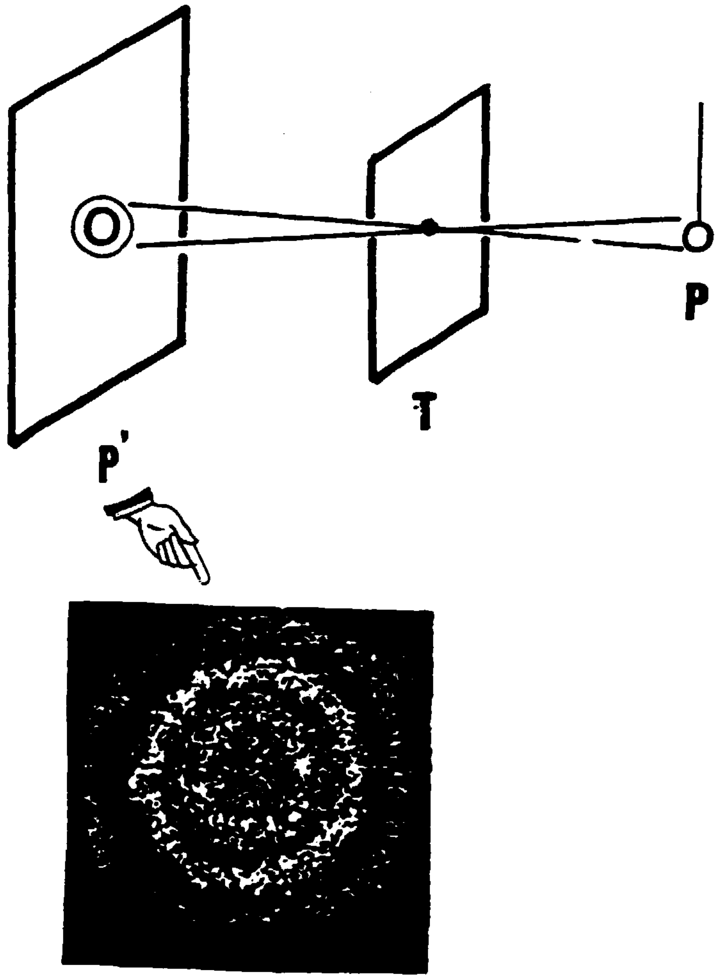

Fig. 3 X-ray pinhole recordings for a bare microballoon 120 μm in diameter.

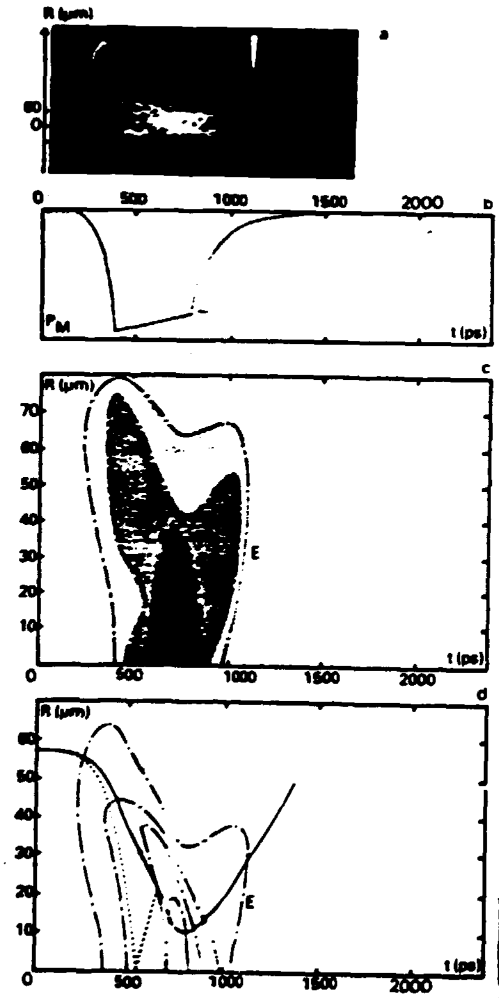

Fig. 4 a) Time resolved X-ray emission for target D ; b) Time scale relative to the incident laser pulse (L) ; c) Graphic interpretation of 4a ; d) Numerical simulation reults ; Broken lines correspond to isodensity contours, at different level.

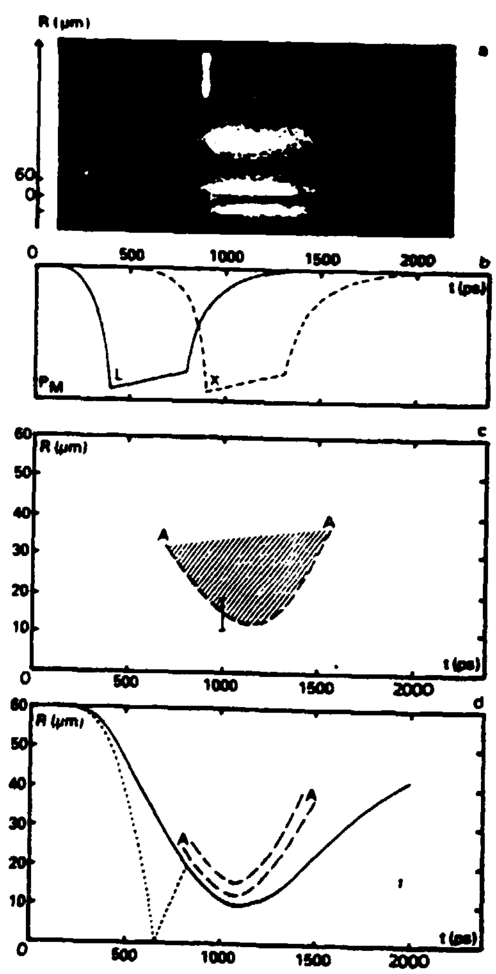

Fig. 5 a) Time resolved X-ray shadowgram obtained with target E (upper signal : X-ray source alone lower signal : X-ray source transmission through the imploding microballoon) ; b) Time scale and relative timing of laser pulse (L) and X-ray source (X) ; c) Graphic interpretation of the absorption contour in a) ; d) Numerical simulation results (—— glass DT interface ; ..... shock ; A‑‑‑Iso transmission $\frac{I}{I_o}$ = 0.1 and 0.2.

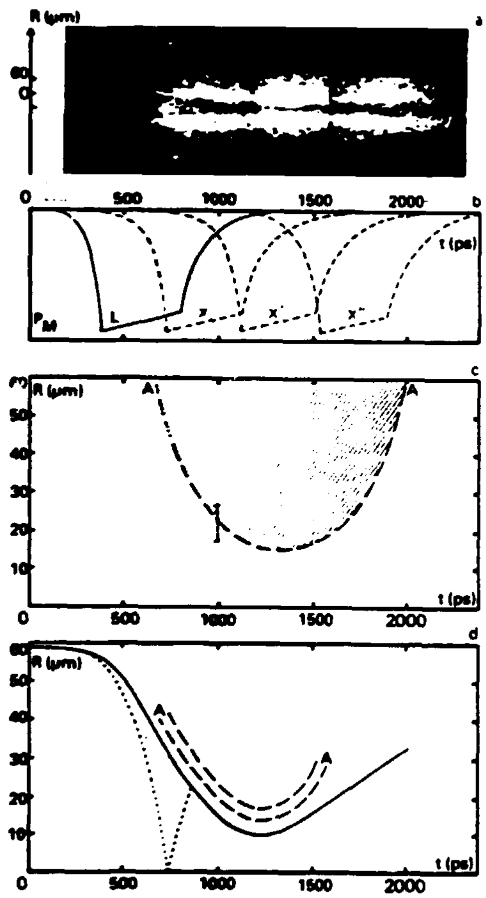

Fig. 6 a) Time resolved X-ray shadowgram obtained with target F (three different shocks) ; b) X-ray source timings for these experiments ; c) Graphic interpretation of the absorption contour in a) ; d) Numerical simulation results (— glass DT interface ;... shock ; A=== iso-transmission $\frac{I}{I_o}$ = 0.1 and 0.2.

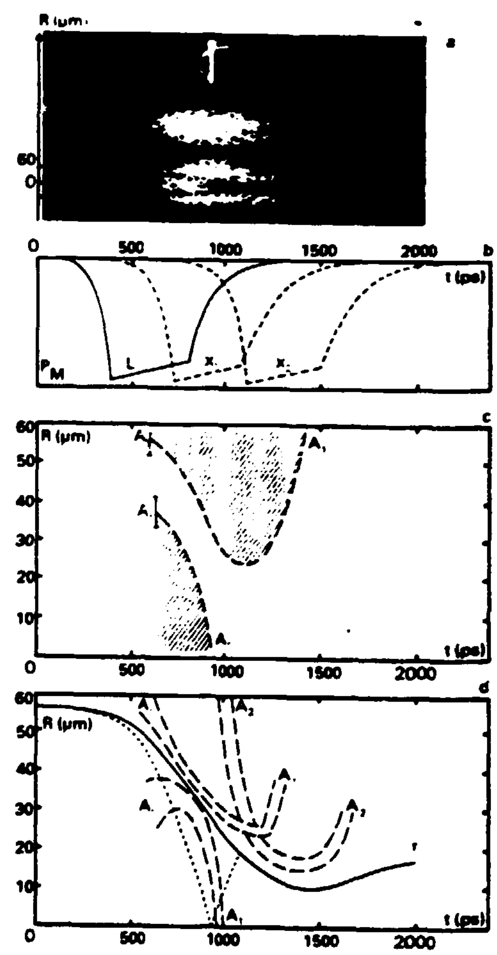

Fig. 7 a) Time resolved X-ray shadowgram obtained with target G (three different shocks) ; b) X_1 : X-ray source timing used in this experiment X_2 : proper X-ray source timing for probing at maximum compression ; c) Graphic interpretation of the absorption contour in a) ; d) Numerical simulation results (— glass DT interface ; ... shock A=== iso-transmission $\frac{I}{I_o}$ = 0.1 and 0.2.

For targets E and F, the X-ray probing time is well fitted and the minimum iso-transmission contour radius occurs at the same time as that of the glass-DT interface (Figs. 5c, 6c).

Experimental curves are well accounted by numerical ones within 100 ps, i.e. within the experimental accuracy. Also the probed region is close to the glass-DT interface, however, the spatial resolution is not sufficient to determine the DT compression.

For target G, the experiment (Fig. 7c) is well restituted (outlines A_1 on Fig. 7d) but the shadowgraphy timing does not allow to probe the implosion during the maximum of compression ; a supplementary delay time of 400 ps would have been necessary, as shown by the iso-contour simulated for Δ = 750 ps (outlines A_2 on Fig. 7d).

Experimental and calculated compression times are presented Fig. 8, versus the equivalent glass shell thickness

$$\Delta R_{SiO2.eq} = \Delta R_{SiO2} + \frac{\rho_{C8H10}}{\rho_{SiO2}} \Delta R_{C8H10} .$$

Excepted target G for which timing was uncorrect, agreement is fairly good.

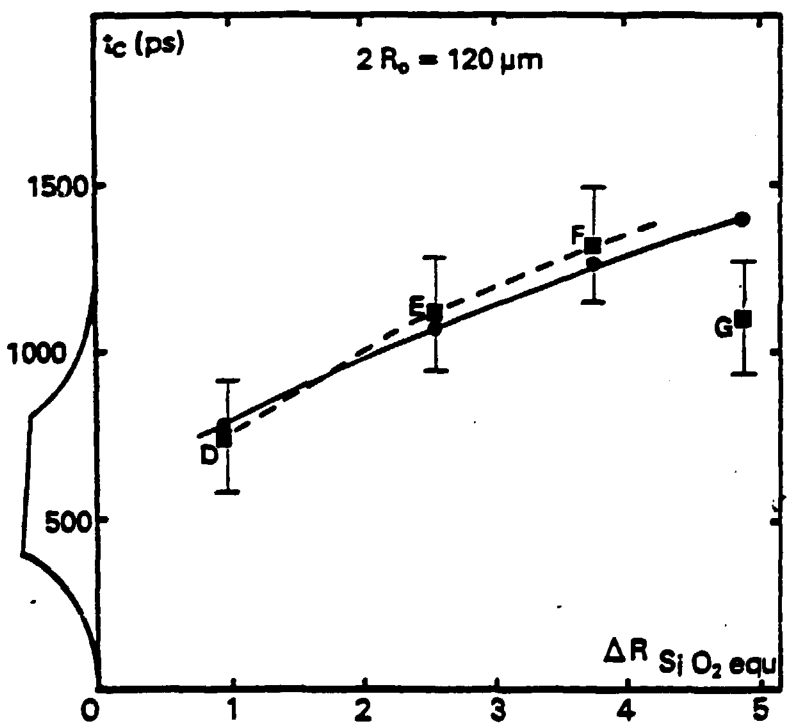

Fig. 8 Comparison of compression time estimated by X-ray shadowgraphy ■ and numerical simulation ● .

Fuel thermodynamical behaviours for the different targets are presented Fig. 9 and 10, as well as temperatures and densities evolutions versus wall thickness (Fig. 11). Highest density ($1.2\ g.cm^{-3}$) is obtained for 5.5 µm plastic coating. At last, compared experimental and simulated neutron yields are shown Fig. 13

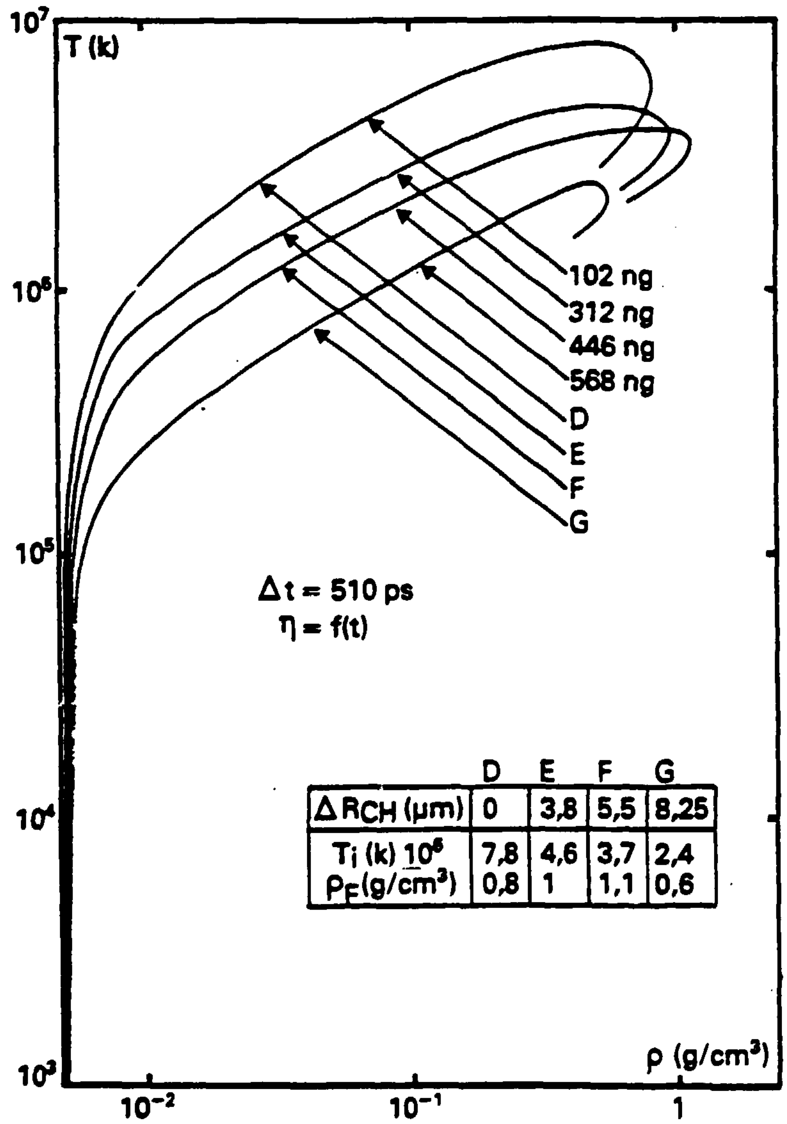

Fig. 9 Fuel thermodynamical evolution for the different targets.

DISCUSSION

Uncertainties in evaluating the target performances are due to both experimental inaccuracy, and crudeness of modeling the physics in the code, particularly the absorption and transport processes. However, all the simulations have been done within identical conditions, and results can be compared as a function of the characteristic parameters of the implosion.

Progress towards a more ablative regime in order to improve ρ_{DT} and $\int\rho dr$, involved :

a) <u>A lowering of the entropy jump in the DT by suprathermal preheat and shock</u>

The level of suprathermal preheat partly depends on the fast electron mean free path compared to the shell thickness ΔR ; it can be reduced by increasing ΔR.

The total preheat in the fuel T_p can be evaluated from the DT thermodynamical diagram, as the starting temperature of the isentropic phase (Fig. 10).

Numerical simulations show that the fraction of incident energy deposited in the fuel by suprathermals decreases when increasing the shell thickness (Table 2) ; in the same times, shock preheat is also reduced as the acceleration is lowered. As a result, T_p decreases from 7.10^5 to 2.10^5 °K (Fig. 10).

Table 2.

ΔR_{C8H10}	$\frac{E_{s.th}}{E_i}$
0	1.5×10^{-4}
3.8	7.4×10^{-5}
5.5	4.7×10^{-5}
8	2.7×10^{-5}

b) <u>To improve the efficiency of following transfers</u> :
Laser energy ⟶ kinetic pusher energy ⟶ Dt internal energy.

Classical ablative acceleration models [36] give an hydrodynamic efficiency $\eta_H \frac{X \cdot Log^2}{1-X}$ where X is the ratio of the final pusher mass to the initial one ; maximum η is obtained for X = .2. However, such a model assumes a stationnary state, which is not reached in our cases : as a matter of fact, transit time of the shock in the pusher is not small compared to the laser pulse duration.

Moreover, η_H depends also on the reaction pressure of the compressed fuel against the pusher, and thus of the suprathermal preheat.

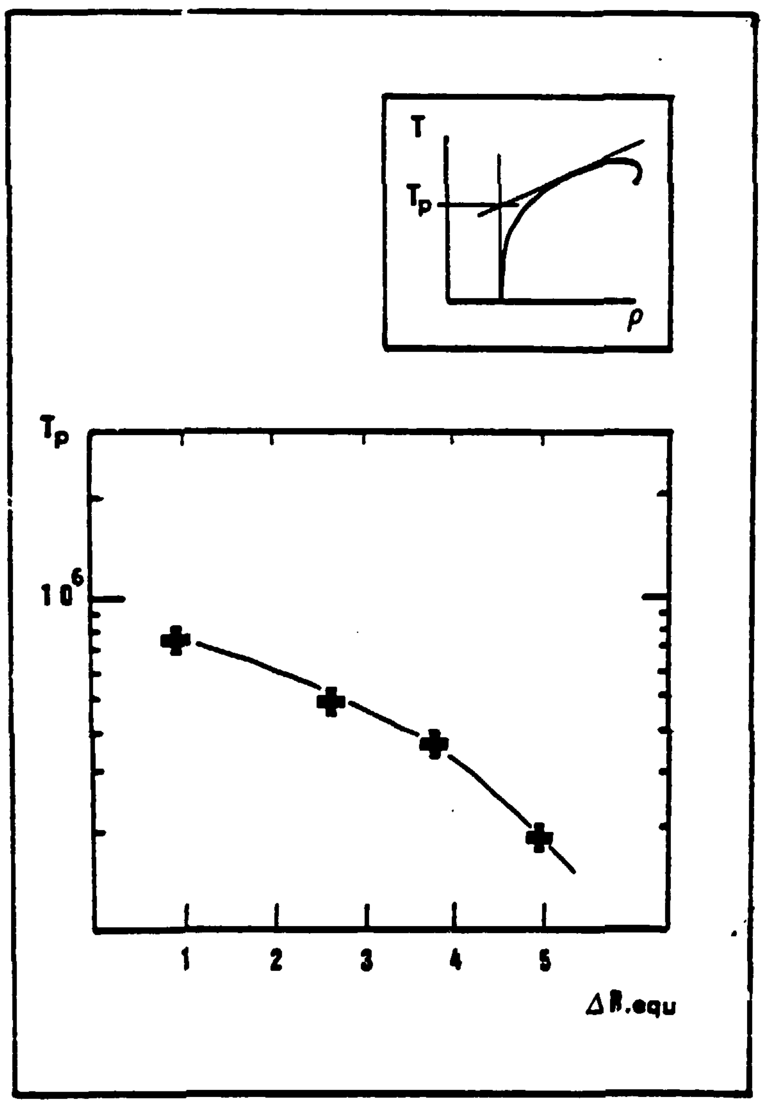

Fig. 10 Preheat temperature T_p versus equivalent shell thickness.

It is the same for the second transfer process, the efficiency of which depends on the preheat of both fuel and pusher.

The evolution of the fractionnal maximum kinetic energy is reported Fig. 12a versus the equivalent shell thickness. This target gets its maximum kinetic energy at nearly the end of the laser pulse (800 ps).

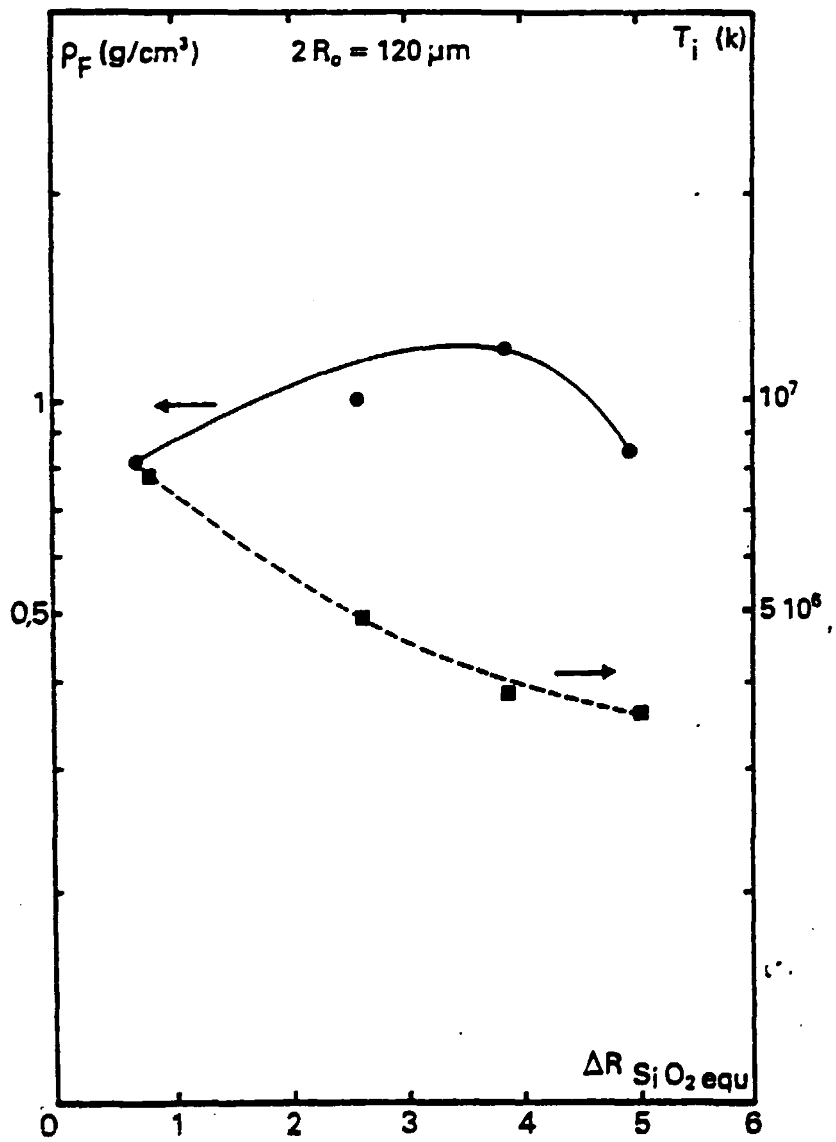

Fig. 11 Final fuel density ● and temperature ■ versus equivalent shell thickness.

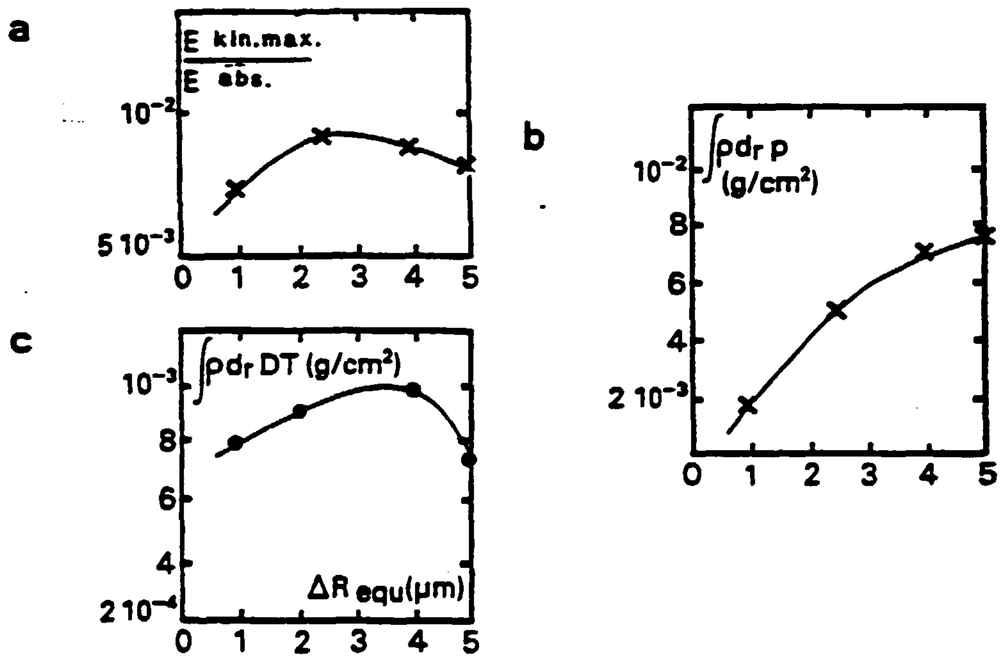

Fig. 12 a) Variation of hydrodynamical efficiency (maximum pusher kinetic energy over absorbed energy) versus equivalent shell thickness
b) and c) Variation of $\int \rho dR$ for the pusher and the fuel.

Compression efficiency and final performances are summarized Figs. 11 and 12. It can be observed that the maximum mean DT temperature decreases when ΔR is increased, while $\bar{\rho}_{DT}$ and $\int_{DT} \rho dR$ present a maximum for $\Delta R_{eq} \simeq 4$ μm ; also $\int_{pusher} \rho dR$ increases with ΔR.

Maxima for fractionnal kinetic energy and $\int_{DT} \rho dR$ are obtained for slightly different wall thicknesses (respectively 3 and 4 μm) ; this can be due to a lower efficiency of the wall for the smaller thickness, as it is then more preheated.

Comparison between experimental and simulated neutron yield needs some comments (Fig. 13), as the second one appears generally greater. Neutron calculations are very sensitive to the physical models included in the codes, particularly those describing the energy transport processes ; thus model uncertainties make simulations unreliable to some extent.

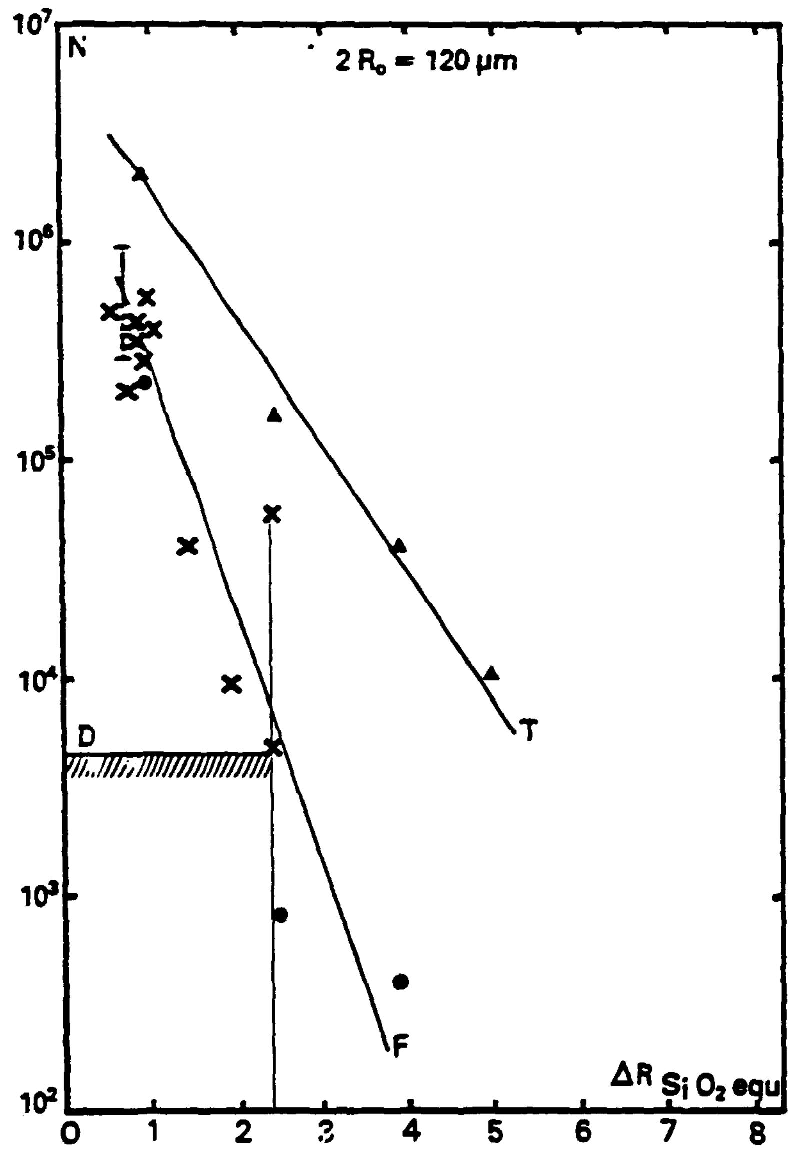

Fig. 13 Variation of the neutron yield versus the equivalent shell thickness

x experimental result

▲ total numerical yields

● numerical yield at shock collapse (first burst).

However, the discrepancy can also be due to other effects ignored by 1D simulations :

- spherical three dimensional large scale effects due to non uniform illumination
- hydrodynamic instabilities
- DT-glass mixing.

From numerical simulations neutron appears to occur in several burst : the first occurs at the initial shock collapse ; the others during the phase of maximum concentrative. In the exploding pusher regime only the first burst exists as slowing down of the pusher is very fast. Neutron emission is then correctly evaluated [32]. On the contrary more ablative implosion shows numerically these several bursts.

In our case, experimental results seem to indicate that only the first burst is observed (Fig. 13).

Such an effect is more clearly evidenced with large diameter high aspect ratio targets ($240 < 2R_0 < 340$ µm ; $100 < \frac{R_0}{\Delta R} < 200$) for with the experimental neutron yield is close to the calculated first burst but about two order of magnitude below the total calculated yield. Disagreement is possibly attributed to upper mentionned effects wich can strongly affect the behaviour of the pusher at the end of compression.

These fondamental issues are addressed in a theoretical paper devoted to the case of large aspect ratio microballoons [37].

CONCLUSION

Implosion studies have been presented, the aim of which were to explore the transition between exploding and ablative regimes. Enhancement of ρ_{DT} and $(\rho R)_{DT}$ has lead to reduce the preheat factors and optimize the laser $\longrightarrow$ fuel energy transfer by imploding thickened targets with intermediate laser pulse (500 ps).

X-ray shadowgraphy has been developped, as a suitable diagnostic for ablative target probing. Numerical simulations have been performed with a 1-D lagrangian code, a particular attention being beared on the description of suprathermal transport.

Increasing the thickness of the target shell has been checked to increase $\int_{pusher} \rho dr$, lower the preheat and induce a more ablative behaviour ; a maximum in final DT density has been observed.

ACKNOWLEDGMENTS

Authors thank the helpfull cooperation of D. Galmiche and J. Launspach ; they acknowledge the contribution of laser manadgement, target fabrication and diagnostic teams ; they are greatly indebted to G. Coulaud, P. Lucas and J. Bouard, H. Croso, J.P. Godefroy, J. Kobus, P. Larousse, J. Turberville for technical assistance.

REFERENCES

1. J. Nuckolls, L. Wood, A. Thissen, G. Zimmerman
Nature 239, 139 (1972).
2. P.M. Campbell, G. Charatis, G.R. Montry
Phys. Rev. Lett. 34, 74 (1975).
3. G.H. Mc Call, T.H. Tan, A.H. Williams
LAUR 75 (1972).
4. E.K. Storm et al.
Phys. Rev. Lett 40, 1570 (1978).
5. A. Bekiarian et al.
AIEA Vienna, 65 (1979).
6. B. Yaakobi et al.
Phys. Rev. A 19, 1247 (1979).
7. C. Bayer et al.
Laser Interaction and Related Plasma Phenomena, Vol. 5, 595 (PPC 1981).
8. E.K. Storm et al.
U.C.R.L. 79. 788 (1977).
9. D. Giovanelli, C.W. Cranfill
LA 7218 (1978).
10. M.D. Rosen and J.M. Nuckolls
Phys. of Fluids, 22, 1893 (1979).
11. B. Ahlborn and M.H. Key
Plasma Physics 23, 435 (1981).
12. E. Fabre et al.
Entropie 89-90, 47 (1979).
13. D.C. Slater at al.
Phys. Rev. Lett. 46, 1199 (1981).
14. H. Nishimura et al.
Phys. Rev. A 23, 2011 (1981).
15. B. Yaakobi et al.
Optics Communications 39, 175 (1981).
16. J.D. Hares et al.
Phys. Rev. Lett. 42, 1218 (1979).
17. J.D. Hares, J.D. Kilkenny
J. Applied Physics, 6420 (1981).
18. F. Amiranoff, R. Fabro, E. Fabre, C. Garban-Labaune, M. Weinfeld
Soumis à Phys. Rev. Lett. (1982).
19. F. Amiranoff et al.
XVth E.C.L.I.M. Schliersee, 1982.

20. D.W. Forslund, J.U. Brackbill
LA.UR 82, 1063.
21. R. Fabro, P. Mora
Phys. Rev. Lett. , Vol. 90A, 48 (1982).
22 C. Bayer et al.
Anomalous Absorption Conference, Santa Fe, (1982).
23. - J. Launspach, D. Billon, M. Decroisette, D. Meynial
Optics Communications 38, 407 (1980).
- D. Billon, J. Launspach, D. Galmiche and D. Meynial
X-ray shadowgraphy studies in laser experiments
VIth International Workshop on Laser Interaction and Related Plasma Phenomena, Monterey 1982
24. E.M. Campbell, W.M. Ploeger, P.H. Lee and S.M. Lane
Appl. Phys. Lett 36, (1980).
25. D. Billon et al.
Laser Interaction and Related Plasma Phenomena, Vol. 4, (PPC 1977).
26. N.G. Basov et al.
Sov. Phys. JETP 51, 212 (1980).
27. A.S. Shikanov
The Journal of Soviet -aser Research, 1, 128 (1980).
28. J.M. Auerbach et al.
Phys. Rev. Lett. 44, 1672 (1980).
29. M.H. key et al.
Phys. Rev. Lett. 45, 1801 (1980).
30. H. Azechi et al.
Technology Reports of the Osaka University, Vol. 30, 157 (1980).
31. M. Bernard et al.
A.P.S. Annual Meeting, Atlanta (1977).
32. Note C.E.A. n° 2163 (1980).
33. Note C.E.A. n° 2230 (1981).
34. L. Spitzer
Physics of fully ionized gases (Wiley-Interscience N.Y. 1967).
35. K.A. Bruckner, R.S. Janda
Nuclear Fusion, 17, n° 6, 1265 (1977).
36. B.H. Ripin et al.
Physics of Fluids, 23, 1012 (1980).
37. J.M. Dufour, D. Galmiche, B. Sitt,
Investigations of hydrodynamic stability of high aspect ratio targets in laser experiments
VIth International Workshop on Laser Interaction and Related Plasma Phenomena.